Numerical and experimental characterization of solid-state micropore-based cytometer for detection and enumeration of biological cells

ARTICLE *in* ELECTROPHORESIS · DECEMBER 2014

Impact Factor: 3.03 · DOI: 10.1002/elps.201400376

Jinhong Guo[1,2]
Liang Chen[1]
Ye Ai[2]*
Yuanbing Cheng[3]
Chang Ming Li[4]
Yuejun Kang[5]
Zhiming Wang[1]

[1]Institute of Fundamental and Frontier Sciences, University of Electronic Science and Technology of China, Chengdu, P. R. China
[2]Pillar of Engineering Product Development, Singapore University of Technology and Design, Singapore
[3]Research Institute of Smart Terminal, Sichuan Changhong Electric Co., Ltd., Sichuan, P. R. China
[4]Institute for Clean Energy & Advanced Materials, Southwest University, Beibei, Chongqing, P. R. China
[5]School of Chemical and Biomedical Engineering, Nanyang Technological University, Singapore

Received July 31, 2014
Revised November 25, 2014
Accepted November 27, 2014

Research Article

Numerical and experimental characterization of solid-state micropore-based cytometer for detection and enumeration of biological cells

Portable diagnostic devices have emerged as important tools in various biomedical applications since they can provide an effective solution for low-cost and rapid clinical diagnosis. In this paper, we present a micropore-based resistive cytometer for the detection and enumeration of biological cells. The proposed device was fabricated on a silicon wafer by a standard microelectromechanical system processing technology, which enables a mass production of the proposed chip. The working principle of this cytometer is based upon a bias potential modulated pulse, originating from the biological particle's physical blockage of the micropore. Polystyrene particles of different sizes (7, 10, and 16 μm) were used to test and calibrate the proposed device. A finite element simulation was developed to predict the bias potential modulated pulse (peak amplitude vs. pulse bandwidth), which can provide critical insight into the design of this microfluidic flow cytometer. Furthermore, HeLa cells (a type of tumor cell lines) spiked in a suspension of blood cells, including red blood cells and white blood cells, were used to assess the performance for detecting and counting tumor cells. The proposed microfluidic flow cytometer is able to provide a promising platform to address the current unmet need for point-of-care clinical diagnosis.

Keywords:
Cell analysis / Flow cytometer / Microelectromechanical system / Microfluidics / Portable diagnosis
DOI 10.1002/elps.201400376

1 Introduction

Circulating tumor cells (CTCs) play a critical role in the cancer metastasis, in which the CTCs detached from the primary tumor tissue spread through blood circulation to distant tissues or organs [1, 2]. These tumor cells have been found in the blood circulation of many cancer patients with metastatic diseases. Since the chance of metastases generally depends on the number density of CTCs spread into the circulation, accurate quantitation of CTCs in the peripheral blood not only can help identify the early sign of cancer, but also can assist in monitoring the disease prognosis and thus improving therapeutic efficacy. However, it is technically highly challenging to detect and count CTCs at the very early stage because of the extremely low concentration, which is on the order of 1∼200 CTCs/mL of whole blood [3, 4].

Microfluidic flow cytometry has established as a powerful technology for multiparametric analysis of biological cells both in fundamental research and clinical applications, especially for cancer detection. Optofluidic cytometry has been introduced to study various cancer cells by comparing three optical signals, namely forward scatter, side scatter, and fluorescence signal; statistical information of cells type, size, and population can be obtained in a few minutes [5–8]. Although very effective, the optofluidic cytometry requires complex optical systems. Resistive pulse sensing is a label-free technique for cell detection and enumeration based on the size and electrical properties of cells. Many different versions of microcytometers based upon electrical impedance detection have also been introduced [9–12]. The working mechanism of the resistive pulse sensor is based on the Coulter principle. When a particle carried by a polar liquid passes a micro-/nanopore, the electrical resistance of the micro-/nanopore will significantly increase due to the physical blockage by the particle, leading to a notable change in the electrical current (a current pulse) through the pore. Every single pulse corresponds to an event of a single particle translocation, and a higher pulse amplitude typically implies a larger particle size. By characterizing the amplitude of the electrical pulses, statistical information of the size and the number distribution of the particles can be obtained. The microfluidic resistive flow cytometry

Correspondence: Professor Jinhong Guo, Institute of Fundamental and Frontier Sciences, University of Electronic Science and Technology of China, Chengdu, 610054, P. R. China
E-mail: guojinhong@uestc.edu.cn

Abbreviations: **CTC**, circulating tumor cell; **EDL**, electrical double layer; **RBC**, red blood cell; **RIE**, reactive ion etching; **WBC**, white blood cell

Colour Online: See the article online to view Figs. 2–5 in colour.

*Additional corresponding author: Professor Ye Ai,
E-mail: aiye@sutd.edu.sg

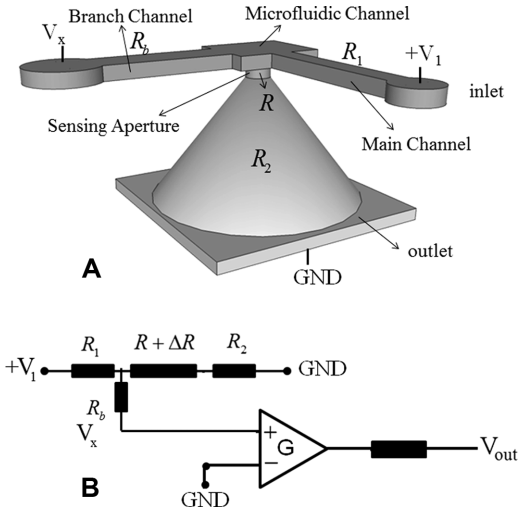

Figure 1. (A) Design of the micropore for resistive pulse sensing. The upper fluidic channel for particle loading is separated from the lower fluidic channel by a small sensing micropore; (B) equivalent electric circuit of the device. ΔR is the change in the micropore's electrical resistance induced by the particle translocation.

could enable an inexpensive solution for rapid and accurate characterization of biological cells [13–18]. It is expected that the next generation of resistive cytometry will be equipped with multiple microfluidic channels that can achieve much higher throughput for screening tumor cells in whole blood samples.

In this paper, we present a design of microfluidic resistive cytometer with a solid-state micropore. Compared to existing studies typically making use of nonstandard techniques for prototyping, the sensing micropore in our device was fabricated on a silicon wafer using a standard microelectromechanical system technology. The microelectromechanical system process could enable mass production of the proposed device that holds great potential to reduce the fabrication cost. The bias voltage modulated pulses induced by polystyrene microparticles of different sizes were simulated and demonstrated for proof-of-concept. This paper systematically presents both numerical and experimental characterization of the particle translocation through a micropore. The numerical simulation shows acceptable agreement with experimental observation, which can provide critical guidance for the development of microfluidic resistive cytometer. We also combine the pulse peak and the translocation time to differentiate tumor cells from blood cells. The developed microfluidic cytometer is compared with a commercial flow cytometer to evaluate the enumeration accuracy of tumor cells.

2 Materials and methods

Figure 1A shows a schematic geometry of the proposed micropore-based cytometer. Particles are released from the upper reservoir and then transported through a small sensing aperture by a pressure-driven flow. Since an electrical potential difference is applied across the micropore, the particle is also subjected to electrophoretic, electroosmotic, and dielectrophoretic effects, in addition to the gravity and buoyant force. As indicated in the equivalent circuit shown in Fig. 1B, once a single microparticle blocks the micropore, the electrical resistance of the pore significantly increases since the electrically nonconducting particle replaces the electrically conducting carrier fluid in the pore. As a result, the bias voltage V_x increases and is thus measured to quantify the resistive pulse.

An axisymmetric model was developed based on a commercially available Finite Element package (COMSOL Multiphysics ® 4.3b; COMSOL, CA, USA). The computational domain includes the upper fluidic channel, the micropore, and the lower fluidic channel. The simulation of particle translocation through the micropore for resistive pulse sensing is implemented by solving the electric field, flow field, and particle motion in a coupled manner. Once the change in the micropore's electrical resistance, ΔR, induced by the particle translocation, is determined by the numerical model, the bias voltage V_x can be calculated from the equivalent circuit shown in Fig. 1B. Thus, this numerical model can characterize the relationship between the change in bias voltage V_x and the volume of the particle through the micropore.

2.1 Theoretical background

The thickness of electrical double layer (EDL) is typically on the order of several nanometers, which is much smaller compared to the particle size or pore size in this study. Therefore, a thin EDL approximation, incorporating the EDL into the charged surface as a single entity, is valid in the modeling of microscale electrokinetics. Therefore, the carrier fluid is a neutral electrolyte solution, and the electrical field is thus governed:

$$\nabla^2\varphi = 0, \tag{1}$$

where φ is the electrical potential. Electrical potentials applied at the inlet and the outlet are $\varphi_{in} = 10\text{V}$ and $\varphi_{out} = 0\text{V}$, respectively. The particle surface and the channel wall are assumed nonconducting and rigid.

Due to the extremely high input impedance of the measurement equipment (on the order of GΩ), the resistance of the branch channel (on the order of MΩ) can be neglected. Therefore, the bias voltage measured by the sensing electrode can be approximately evaluated by the average voltage at the intersection between the branch and the main channel,

$$\overline{V_x} = \frac{\int \varphi d\,S}{\int 1 d\,S}. \tag{2}$$

Here, S is any cross-section of the branch channel.

The flow field in the computational domain is governed by the Navier–Stokes equation:

$$\rho\left(\frac{\partial \vec{u}}{\partial t} + \vec{u}\cdot\nabla\vec{u}\right) = -\nabla p + \mu\nabla^2\vec{u}, \tag{3}$$

and the continuity equation:

$$\nabla \cdot \vec{u} = 0, \tag{4}$$

where $\vec{u}$ is flow field, ρ is the fluid density, p is the pressure, and μ is the dynamic viscosity.

Under the thin EDL approximation, the electroosmotic flow induced by charged surfaces can be described by Smoluchowski slip velocity [19,20]. Therefore, the velocity boundary condition at the channel wall is given by:

$$\vec{u} = \frac{\varepsilon_0 \varepsilon_r \zeta_w}{\mu} \left(\bar{\bar{I}} - \vec{n}\,\vec{n} \right) \cdot \nabla \varphi. \tag{5}$$

As the particle is moving, the boundary condition at the particle surface is given by the summation of the particle velocity and the electroosmotic flow velocity,

$$\vec{u} = \vec{V}_p + \frac{\varepsilon_0 \varepsilon_r \zeta_p}{\mu} \left(\bar{\bar{I}} - \vec{n}\,\vec{n} \right) \cdot \nabla \varphi, \tag{6}$$

where ε_0 and ε_r are the absolute permittivity of vacuum and the relative permittivity of fluid, respectively, ζ_p and ζ_w are the zeta potential of the particle and the channel wall, respectively, $\vec{V}_p$ is the translocation velocity of the particle, and $(\bar{\bar{I}} - \vec{n}\vec{n}).\nabla\varphi$ defines the electrical field tangent to the charged surface with $\bar{\bar{I}}$ and $\vec{n}$, indicating the second-order unit tensor and the unit normal vector, respectively. A volumetric flow rate is specified at the inlet, while the pressure at the outlet is assumed zero.

As a result of the pressure-driven flow and an external potential difference applied across the micropore, the particle starts to transport from the inlet to the outlet. The particle motion is governed by the Newton's second law,

$$m_p \frac{d\vec{V}_p}{dt} = \vec{F}_{net}, \tag{7}$$

where m_p is the mass of the particle and $\vec{F}_{net}$ is the net force acting on the particle. The net force is composed of the following forces: the electrical force $\vec{F}_E$, the hydrodynamic force $\vec{F}_h$, the buoyant force, and gravity force. As a result, the total net force is described by:

$$\vec{F}_{net} = \vec{F}_E + \vec{F}_h + (\rho_p - \rho) V g, \tag{8}$$

where ρ_p is the particle density and V is the particle volume. The electrical force including the electrophoretic force and dielectrophoretic force is obtained by integrating the Maxwell stress tensor, $\bar{\bar{\sigma}}_E$, over the particle surface [19–22],

$$\vec{F}_E = \oiint \bar{\bar{\sigma}}_E \cdot \vec{n}\, d\Gamma = \oiint \left[\varepsilon_0 \varepsilon_r \vec{E}\,\vec{E} - \frac{1}{2} \varepsilon_0 \varepsilon_r \left(\vec{E} \cdot \vec{E} \right) \bar{\bar{I}} \right] \cdot \vec{n}\, d\Gamma, \tag{9}$$

where Γ is the particle surface and $\vec{E}$ is the electric field derived from the electric potential by $\vec{E} = -\nabla\varphi$. Due to the thin EDL approximation, the surface charge of the particle is neutralized by the counter ions within the EDL that results in the local zero charge density, referring to a nonconducting surface. As a result, the first term of the integrand in the right hand side of Eq. (9), $\varepsilon_0 \varepsilon_r \vec{E}\,\vec{E} \cdot \vec{n}$, is zero. The hydrodynamic force acting on the particle, taking into account both the pressure-driven flow and the electroosmotic flow, is calculated by integrating the hydrodynamic stress tensor, $\bar{\bar{\sigma}}_H$, over the particle surface [19–22],

$$\vec{F}_H = \oiint \bar{\bar{\sigma}}_H \cdot \vec{n}\, d\Gamma = \oiint \left[-p\bar{\bar{I}} + \mu[\nabla \vec{u} + (\nabla \vec{u})^T] \right] \cdot \vec{n}\, d\Gamma. \tag{10}$$

The initial position and velocity of the particle are set to $\vec{X}_p \big|_{t=0} = \vec{X}_{p0}$ and $\vec{V}_p \big|_{t=0} = 0$, respectively.

The aforementioned governing equations are defined in an arbitrary Lagrangian–Eulerian frame, in which the particle motion is tracked in a Lagrangian manner while the electric field and flow field are solved in an Eulerian manner. The mesh is able to deform to capture the new location of the particle after each computational step. When the mesh quality degrades to a specific level that may compromise the computational accuracy, a remeshing is implemented to generate a new geometry with undeformed mesh to continue the particle tracking until the particle translocates through the micropore. This model has been previously applied to simulate pressure-driven particle motion [23] and electrokinetic particle motion in various microchannels [24–27]. All the parameters in this study are summarized in Table 1.

Table 1. Parameters used in the numerical modeling

Parameter	Value
Absolute permittivity of vacuum (F/m)	8.8542×10^{-12}
Relative permittivity of water	80
Zeta potential of particle (mV)	−40
Zeta potential of micropore (mV)	−50
Density of fluid (kg/m^3)	998
Density of particle (kg/m^3)	1050
Viscosity of fluid (kg/(m·s))	1.0×10^{-3}
Inlet flow rate (μL/min)	1.5

2.2 Device fabrication

As illustrated in Fig. 2A, the micropore was fabricated on an 8-inch silicon wafer, which was predeposited with 20 μm SiO_2 as the dielectric layer. There were three lithography steps. The first step was to etch the micropore of 20 μm in diameter from the top side. After spin coating with a 2 μm thick thin film photoresist (UV26-2.5; Dow Chemicals, Singapore), the device was exposed to UV light to open the etching area. Reactive ion etching (RIE) was used to etch the 20 μm dielectrics of the chip and deep RIE was further used to etch 10 μm into silicon. After etching, photoresist was removed and the wafer was cleaned. Then, the wafer was deposited with 100 nm SiO_2 and 150 nm of Si_3N_4 using plasma-enhanced chemical vapor deposition as a protection layer for the subsequent processing. The wafer was thinned down to around 400 μm by back

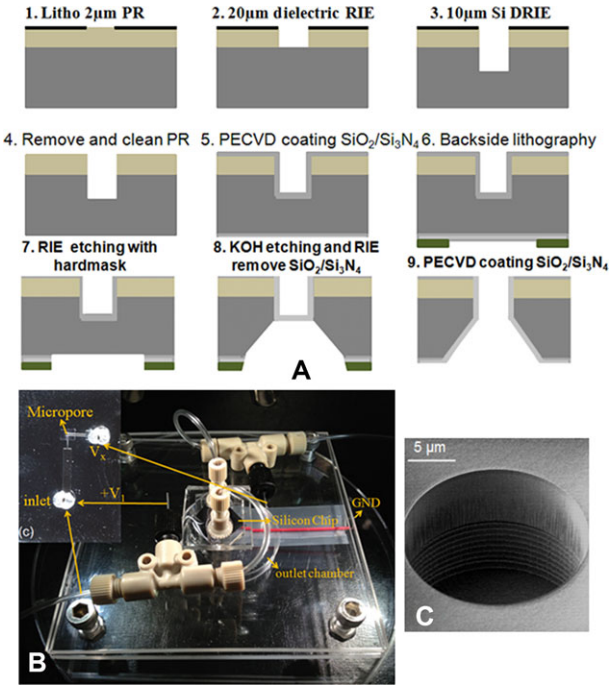

Figure 2. (A) Fabrication procedure of the micropore on a silicon wafer; (B) experimental setup; (C) A SEM image of the etched structure: a sensing aperture of 20 μm in diameter and 30 μm in length.

grinding. The second lithography was used to etch the pore from the back side of the wafer. SiO_2/Si_3N_4 were deposited on the backside as hard mask for the backside etching. After photoresist coating and UV exposure from the backside, RIE was used to etch the SiO_2/Si_3N_4 hard mask to expose the silicon, followed by wet etching of silicon using KOH. Then, the remaining SiO_2/Si_3N_4 protection layer for the front side, which blocked the pore, was removed by buffered oxide etching and H_3PO_4 etching. Finally, the whole wafer, including the interior side of the pore, was coated with SiO_2/Si_3N_4. The wafer was diced and the fabricated micropore was then connected to three reservoirs for the fluidic interface (the inlet, outlet, and bias reservoirs as shown in Fig. 1A). The reservoirs were fabricated by PDMS using a standard soft lithography technique [28], and then permanently bonded onto the diced wafer after plasma treatment. Figure 2B shows the experimental setup of the device, and Fig. 2C shows a SEM image of the etched micropore.

2.3 Measurement setup

The samples were injected through the inlet reservoir by a syringe pump and the waste was removed from the outlet reservoir. Each reservoir was placed with a platinum wire. The platinum wires placed in the inlet and outlet reservoirs were used to apply the electric potential difference, while the platinum wire placed in the side branch reservoir was used to measure the bias voltage, V_x, for signal readout. Once the PBS solution saturates all the channels, the side branch reservoir was sealed to prevent leakage. Consequently, the sample can only flow through the micropore to the outlet reservoir. The bias voltage of the side branch channel was monitored under a total bias of 10 V across the entire fluidic channel by using a patch clamp amplifier (EPC10 USB Quadro, HEKA Electronik, Lambrecht, Germany), which provided accurate detection of the small voltage modulation with high S/N. The data were collected and imported into a homemade MATLAB program for postprocessing.

3 Results and discussion

3.1 Peak amplitude and translocation time

Polystyrene particles of various sizes (7, 10, and 16 μm) were used to calibrate the electric voltage modulation of the side branch and also validate our numerical modeling. A good linearity with regression of $R^2 = 0.999$ was achieved by comparing the measured relative peak amplitude of the voltage pulses to the volume of the particles, as shown in Fig. 3A. Our experimental results show that the voltage modulation amplitude is linearly proportional to the particle volume, which is also confirmed in the simulation. Figure 3B shows the pulse bandwidth (translocation time) induced by the three polystyrene particles of different sizes. It is revealed that

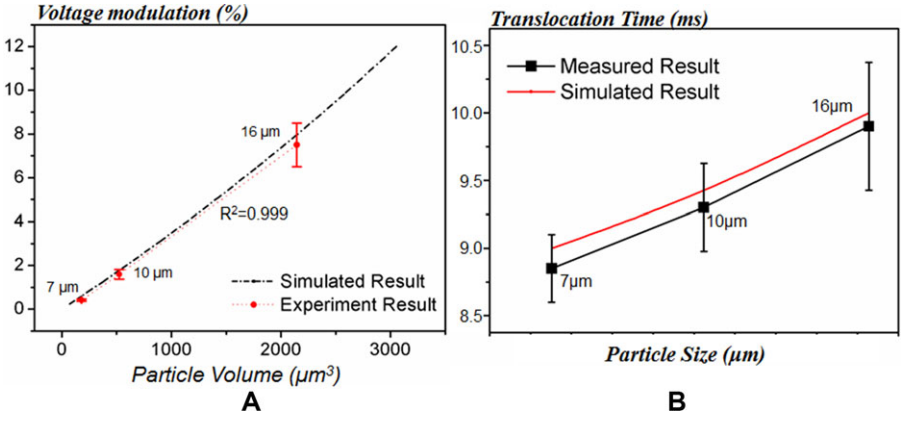

Figure 3. (A) Electric voltage modulation as a function of the particle volume. The peak amplitude is evaluated as a percentage modulation based on the baseline voltage at the branch channel. The dotted line is a linear regression of the experimental data; (B) comparison between the numerical predictions and experimental results of pulse bandwidth induced by polystyrene particles of different sizes.

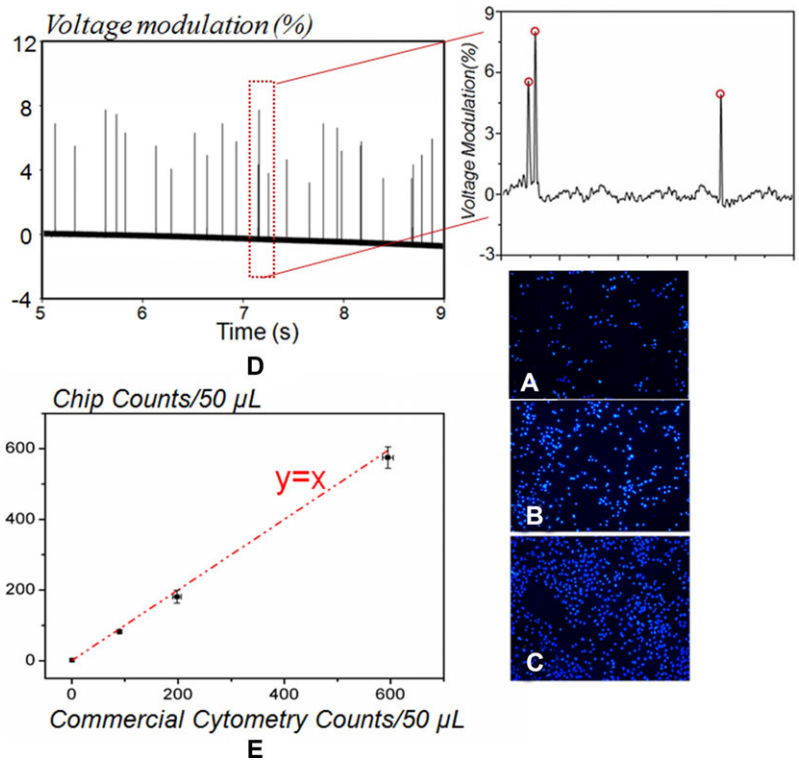

Figure 4. Fluorescence microscopic images of different concentrations of stained HeLa cells: (A) 2×10^3 mL^{-1}, (B) 4×10^3 mL^{-1}, and (C) 1.2×10^4 mL^{-1}, (D) continuous monitoring of bias voltage of the branch channel. Each spike indicates a single detected cell; (E) comparison of HeLa cell enumeration by the fabricated device and a commercial flow cytometer.

larger particles have a wider pulse bandwidth (longer translocation time) than smaller particles, which implies that they move slower than smaller particles through the micropore. This phenomenon is mainly attributed to the size-dependent wall retardation effect, which has also been confirmed in our previous studies [23]. In addition, the experimental result of particle-induced pulse bandwidth shows a good agreement with the numerical simulation. It is concluded that microparticles of different sizes can be differentiated by correlation analysis of pulse peak amplitude and pulse bandwidth, which is also helpful information for the differentiation of tumor cells from blood cells.

3.2 Cell detection and enumeration

In order to quantitatively evaluate the accuracy of cell enumeration, specific concentrations of HeLa cells (Fig. 4A–C) were tested using both the fabricated device and a commercial cytometer. A series of typical resistive pulse signals for the detection of HeLa cells is shown in Fig. 4D. Each resistive pulse indicates a tumor cell event and the pulse amplitude is proportional to the cell volume. The comparison of both results is shown in Fig. 4E, which shows a good accuracy of the developed device as compared to the commercial cytometer. This study demonstrates that the presented solid-state micropore-based cytometer is able to provide a reliable platform for cell detection and enumeration, such as analysis of tumor cells, which is a promising methodology for future point-of-care diagnosis, especially in the resource-limited developing countries.

3.3 Detection of tumor cells from a heterogeneous cell sample

In order to investigate the performance of the developed microfluidic cytometer for the detection of tumor cells in heterogeneous cell samples, a mixture of red blood cells (RBCs) (1000 cells/mL), white blood cells (WBCs) (1000 cells/mL), and HeLa cells (3000 cells/mL) was used to flow through the device for quantitative evaluation. Before the cell differentiation experiment using a heterogeneous sample, each cell type was tested through the same device to characterize their voltage modulations. This characterization process was performed to define classification boundaries between the three cell populations, which were subsequently used for differentiating cells in the heterogeneous sample. The averaged size of RBCs (equivalent to a microsphere), WBCs, and HeLa cells are 5, 10, and 15 μm. Due to the large difference in the cell size, it is expected that they will have distinct electric voltage modulation. As discussed previously, the translocation time depends on the cell size as well due to the size-dependent wall retardation effect. In addition, different cells have distinct physiological properties, which may lead to unique surface charge that can be characterized by zeta potential. It has been experimentally measured that RBCs, WBCs, and HeLa cells have a significant difference in zeta potential [29], which results in different electrophoretic mobility.

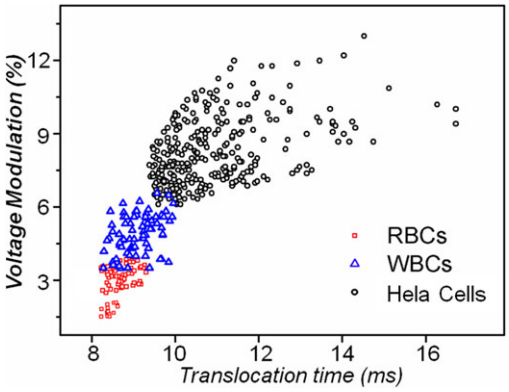

Figure 5. Scatter plot of the peak amplitude and translocation time for a mixed cell sample including RBCs, WBCs, and HeLa cells.

Therefore, the translocation time of a single cell, calculated from the analysis of the modulated pulse bandwidth, is able to provide another important parameter to differentiate biological cells. Consequently, the correlation spectroscope by two parameters, pulse amplitude and translocation time, can be concurrently analyzed for more accurate determination of different cell types.

Figure 5 shows the voltage modulation versus translocation time scatter plot of the mixed cell sample with a total 483 cell events through the micropore. To accurately differentiate cells in the overlapping region, data points falling near the preobtained classification boundaries were confirmed by the microscopic images of cells after passing through the micropore. As explained earlier, RBCs induce smaller peak amplitude than WBCs and HeLa cells, due to the fact that HeLa cells and WBCs have a larger size resulting in a greater current blockage of the sensing aperture. Similarly, the peak amplitude induced by WBCs is smaller than HeLa cells because of a smaller size compared to HeLa cells. Figure 5 also reveals a clear contrast in the translocation time between the three different cell types, which is mainly attributed to the difference in size and zeta potential. Therefore, the correlation between peak amplitude and translocation time can effectively differentiate the three cell types. This proof-of-concept study demonstrates that the proposed device is able to provide important information that can help distinguish tumor cells from blood cells, which might contribute to more practical applications of detecting extremely rare CTCs from the highly complex background of the whole blood.

4 Concluding remarks

In this paper, we demonstrated a micropore-based cytometer for tumor cell detection and enumeration by characterizing their resistive pulse profiles. The presented numerical model is able to predict the voltage modulation induced by the translocation of individual bioparticles, providing critical insight for the systematic design of this microfluidic cytometer. Furthermore, the experimental results have shown that tumor cells can be detected and enumerated from a heterogeneous cell sample by the proposed device with acceptable efficiency and accuracy as compared to a commercial flow cytometer. Therefore, this device is a promising and cost-effective platform for rapid point-of-care detection and enumeration of specific cell types.

This research is supported by a seed grant from Sustainable Earth Office at Nanyang Technological University and Tier-1 Academic Research Fund from Singapore Ministry of Education (RG 26/11) awarded to Y.K. and SUTD-MIT International Design Center IDG11300101 awarded to Y.A.

The authors have declared no conflict of interest.

5 References

[1] Wang, X., Qian, X., Beitler, J. J., Chen, Z. G., Khuri, F. R., Lewis, M. M., Shin, H. J. C., Nie, S., Shin, D. M., *Cancer Res.* 2011, *71*, 1526–1532.

[2] Kohn, E. C., Liotta, L. A., *Cancer Res.* 1995, *55*, 1856–1862.

[3] Allard, W. J., Matera, J., Miller, M. C., Repollet, M., Connelly, M. C., Rao, C., Tibbe, A. G., Uhr, J. W., Terstappen, L. W. *Clin. Cancer Res.* 2004, *10*, 6897–6904.

[4] Paterlini-Brechot, P., Benali, N. L. *Cancer Lett.* 2007, *253*, 180–204.

[5] Hamish, C. H., James, S. W., *Microfluid. Nanofluid.* 2008, *4*, 53–79.

[6] Yu, J. Q., Liu, X. F., Chin, L. K. Liu, A. Q., Luo, K. Q., *Lab Chip* 2013, *13*, 2693–2700.

[7] Guo, J., Ma, X., Menon, N.V., Li, C. M., Zhao, Y., Kang, Y., *IEEE J. Sel. Top. Quant. Electronics.* 2015, *21*, 7100107.

[8] Lee, G.-B., Lin, C.-H., Chang, G.-L., *Sens. Actuators, A* 2003, *103*, 165–170.

[9] Guo, J., Li, C. M., Kang, Y., *Biomed. Microdevices* 2014, *16*, 681–686.

[10] Guo, J., Li, H., Chen, Y., Kang, Y., *IEEE Sensors J.* 2014, *14*, 2112–2117.

[11] Cheung, K. C., Di Berardino, M., Schade-Kampmann, G., Hebeisen, M., Pierzchalski, A., Bocsi, J., Mittag, A., Tarnok, A., *Cytometry A* 2010, *77A*, 648–666.

[12] Sun, T., Morgan, H., *Microfluid. Nanofluid.* 2010, *8*, 423–443.

[13] Guo, J., Pui, T. S., Ban, Y., Rahman, A. R. R., Kang, Y., *IEEE Trans. Biomed. Eng.* 2013, *60*, 3269–3275.

[14] Holmes, D., Pettigrew, D., Reccius, C. H., Gwyer, J. D., van Berkel, C., Holloway, J., Davies, D. E., Morgan, H., *Lab Chip* 2009, *9*, 2881–2889.

[15] Holmes, D., Morgan, H., *Anal. Chem.* 2010, *82*, 1455–1461.

[16] Bernabini, C., Holmes, D., Morgan, H., *Lab Chip* 2011, *11*, 407–412.

[17] Emaminejad, S., Javanmard, M., Dutton, R. W., Davis, R. W., *Lab Chip* 2012, *12*, 4499–4507.

[18] Evander, M., Ricco, A. J., Morser, J., Kovacs, G. T., Leung, L. L., Giovangrandi, L., *Lab Chip* 2013, *13*, 722–729.

[19] Wu, Y., James, D. B., Mahmoud, A., *Biomed. Microdevices* 2012, *14*, 739–750.

[20] Guo, J., Pui, T. S., Rahman, A. R. R., Kang, Y., *Electrophoresis* 2013, *34*, 417–424.

[21] Guo, J., Lei, W., Ma, X., Xue, P., Chen, Y., Kang, Y., *IEEE Trans. Biomed. Circuits Syst.* 2014, *8*, 35–41.

[22] Wu, Z., Gao, Y., Li, D., *Electrophoresis* 2009, *30*, 773–781.

[23] Ai, Y., Joo, S. W., Jiang, Y., Xuan, X., Qian, S., *Biomicrofluidics* 2009, *3*, 022404.

[24] Ai, Y., Joo, S. W., Jiang, Y., Xuan, X., Qian, S., *Electrophoresis* 2009, *30*, 2499–2506.

[25] Ai, Y., Beskok, A., Gauthier, D. T., Joo, S. W., Qian, S., *Biomicrofluidics* 2009, *3*, 044110.

[26] Ai, Y., Park, S., Zhu, J., Xuan, X., Beskok, A., Qian, S., *Langmuir* 2010, *26*, 2937–2944.

[27] Ai, Y., Mauroy, B., Sharma, A., Qian, S., *Electrophoresis* 2011, *32*, 2282–2291.

[28] Xia, Y. N., Whitesides, G. M., *Annu. Rev. Mater Sci.* 1998, *28*, 153–184.

[29] Bondar, O. V., Saifullina, D. V., Shakhmaeva, II, Mavlyutova, II, Abdullin, T. I., *Acta Nat.* 2012, *4*, 78–81.

